This article has been accepted for inclusion in a future issue of this journal. Content is final as presented, with the exception of pagination.

Analysis of Process Variations in *W*-Band GaN MMIC PAs Using Nonparametric Statistics

Shane Verploegh, *Member, IEEE*, Mauricio Pinto, *Member, IEEE*, Laila Marzall, *Graduate Student Member, IEEE*, Daniel Martin, *Student Member, IEEE*, Gregor Lasser, *Member, IEEE*, and Zoya Popović, *Fellow, IEEE*

***Abstract*— This article presents an analysis of the effects of amplifier process-related performance variation on the radiation patterns of a *W*-band active transmit antenna array. Based on measured on-wafer *S*-parameters for about 80 amplifier chips designed in an experimental 90-nm gallium nitride (GaN) on SiC process, a statistical analysis of the array patterns is performed. Several types of probability density functions (pdfs) are generated from measured data and compared to determine which statistical approach is most relevant. We find that a joint distribution that maintains the correlation structure between $|S_{21}|$ and $\angle S_{21}$ is important for an accurate analysis. The monolithic microwave integrated circuits (MMICs) are connected to the waveguide-fed horn antenna elements in the array via microstrip-to-waveguide transitions fabricated on alumina. The transitions are analyzed in full-wave simulations with fabrication tolerances included in the analysis. Finally, the MMIC and transition statistical variations are cascaded, resulting in a quantitative evaluation of spatial power combining. Given a random choice of power amplifier chips in a 4 × 4 array, the EIRP is shown to vary by ±3 dB at 94 GHz.**

***Index Terms*— Gallium nitride (GaN) amplifier monolithic microwave integrated circuits (MMICs), Gaussian, horn antenna, kernel density estimation, Markov chain Monte Carlo (MCMC), microstrip to waveguide transition, power combining, probability density, *W*-band.**

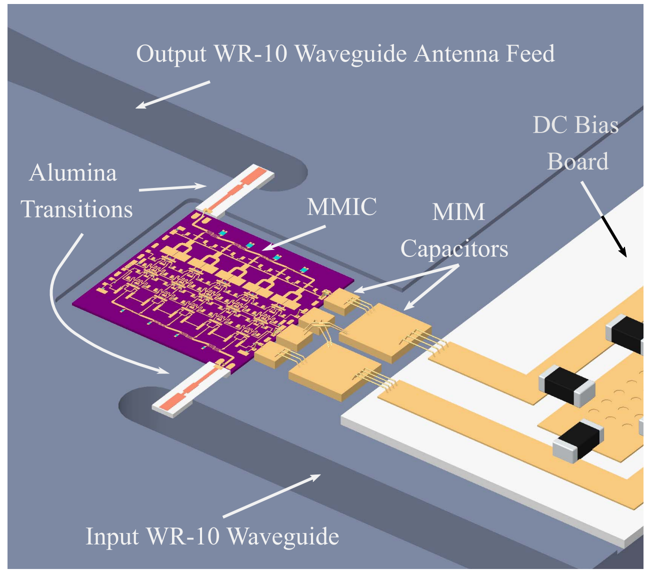

Fig. 1. Image of *W*-band MMIC PAs with bias circuit, microstrip-to waveguide alumina transitions, and input/output WR-10 waveguides.

I. INTRODUCTION

MILLIMETER-WAVE applications above Ka-band are becoming increasingly important due to the heavily used spectrum at lower microwave frequencies. For example, there are new 5G unlicensed allocations at the V-band in the 57–64- and 64–71-GHz bands [1], [2]. High data rate communication systems operating at 92 GHz and achieving 6.5 Gb/s with quadrature amplitude modulation (QAM)-128 were demonstrated in gallium nitride (GaN) [3], and data rates up to 80 Gb/s with 16-QAM signals were shown in a 6-m range wireless 75-GHz link using 100-nm InGaAs mHEMT technology [4]. Low-power *W*-band phased arrays using silicon technology were demonstrated for automotive radar and imaging, [5]–[7], while a 3-D imaging 100-GHz MIMO FMCW radar is investigated in [8].

To achieve transmitters with high effective isotropic radiated power (EIRP) at millimeter-wave frequencies, spatial power combining arrays are of interest, e.g., [9]. Here, we consider an architecture in which each element is fed by a monolithic microwave integrated circuit (MMIC) amplifier, as shown in Fig. 1, with the detail of the multistage power amplifier chip, bias circuitry, and transitions to WR-10 input and output waveguides. The three-stage MMIC PA is implemented in GaN on SiC with power combining of 30 transistors for a peak output power approaching 1 W.

Due to the short gate sizes in the tens of nm range, as well as complex heterostructures, millimeter-wave GaN processes exhibit variations larger than their lower frequency microwave counterparts. The goal of this article is to provide an analysis and understanding of the effects of variations in millimeter-wave GaN MMIC PAs on the overall performance of a transmit array. The statistical analysis process flow consists of data collection, estimation of a probability density function (pdf), sampling from the estimated pdf, and the subsequent application of the samples to a stated problem.

Manuscript received October 13, 2020; revised December 11, 2020, December 29, 2020, and January 15, 2021; accepted January 17, 2021. This work was supported in part by ONR under Contract N00014-15-1-2111 and in part by DARPA under ONR Award N00014-19-1-2236. The work of Zoya Popović was supported by the Lockheed Martin Endowed Chair of RF Engineering, University of Colorado Boulder. *(Corresponding author: Shane Verploegh.)*

Shane Verploegh, Laila Marzall, Gregor Lasser, and Zoya Popović are with the Department of Electrical, Computer, and Energy Engineering, University of Colorado Boulder, Boulder, CO 80309 USA (e-mail: shane.verploegh@colorado.edu).

Mauricio Pinto and Daniel Martin are with the Raytheon Space and Airborne Systems, El Segundo, CA 90245 USA.

Color versions of one or more figures in this article are available at https://doi.org/10.1109/TMTT.2021.3058270.

Digital Object Identifier 10.1109/TMTT.2021.3058270

Here, we perform this statistical analysis for a portion of a transmit chain, taking into account the measured variations in MMIC PAs and simulated variations in transitions from microstrip-to-waveguide antenna feeds. We fit and estimate the marginal and bivariate pdfs of measured amplifier small-signal amplitude and phase of S_{21}, comparing two methods (Gaussian and kernel estimation). A cascaded matrix approach allows extension to additional components in the transmit chain that might contribute to variations, such as antenna element fabrication tolerances and driver amplifier gain variations.

Another possible use of the presented analysis is in calibration of large phased array, especially at millimeter-wave frequencies where MMIC process variations often require pretesting of the die, e.g., [3] and [10]. Most calibration techniques require a setup that provides high degree of phase and amplitude accuracy and necessary functionality in beamforming architectures to apply fine calibration resolution [11]–[13]. The analysis here can provide insight into the need for pretesting of PAs, given a range and accuracy of available phase shift and variable gain required for correction in the calibration steps. Advance knowledge of the gain amplitude and phase can inform the decision related to costly preselection of MMICs or the need for bias control across the transmit array, which will affect the EIRP.

The outline of this article is given as follows. Section II gives specifics of the MMIC PA design and a measured data set across three wafers, revealing correlation of various parameters due to fabrication. Section III initially idealizes sample data with normal/Gaussian distributions for both univariate and bivariate cases as independent random variables and then presents a kernel density estimation method that better describes the data set. Section IV discusses using the pdf estimates in an algorithm for repeated sampling. A *W*-band chip transition to waveguide is simulated with a fabrication and packaging tolerance study in Section V. Section VI shows that the pdfs estimated from a 4-D kernel density scheme can be used in a cascaded topology by compounding error. Finally, in Section VII, the analysis is applied to a spatial power combining array of *E*-plane horns each fed by an MMIC chosen independently and identically from the probability densities estimates.

II. *W*-Band MMIC PA

State-of-the-art GaN millimeter-wave power amplifiers include a traveling wave amplifier with 2.5-W output power and a 13.9-dB gain from 75 to 100 GHz using a 140-nm T2 HRL process [14]. In this T-gate HRL process, there has been significant effort devoted to HEMT scaling [15]. A four-stage PA with greater than 30-dB gain and 1.2-W output power across 72 to 90 GHz has been demonstrated in a 90-nm Qorvo process [16]. Two GaN MMIC PAs demonstrated 400-mW output power with greater than 10-dB gain at 91 GHz in a 100-nm Fraunhofer process [17]. A two-stage cascaded architecture PA showed 1.15-W maximum output power with 18.9-dB maximum gain and 77.8–90 GHz in an 80-nm Fujitsu GaN process [18]. Three *W*-band GaN MMIC PAs fabricated in a 150-nm Raytheon process demonstrated 21-dB gain at 95 GHz, 37% PAE at 91 GHz, and 1.7 W at 91 GHz [19]. A GaN-based 92-GHz phased array with output power as high as 7 kW from was demonstrated for an active denial system [9].

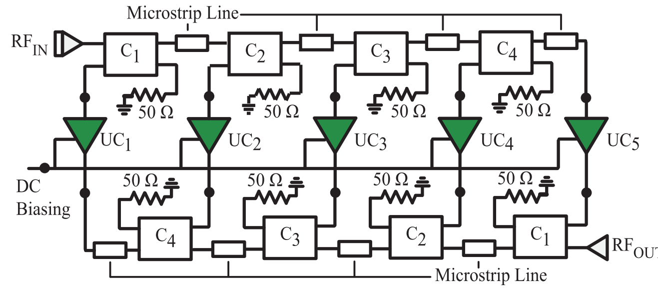

Fig. 2. Circuit block diagram of the chain power amplifier architecture with five UC three-stage PAs connected through Lange couplers. All five UCs are biased from the same voltage supplies.

Here, we describe briefly a GaN MMIC PA in Fig. 1 designed for around 1-W output power across the 75–110-GHz frequency range, as detailed in [20]. The circuit architecture is shown in Fig. 2 and is a five-element chain amplifier similar to that in [14]. The number of sections, $n = 5$, is chosen to achieve 1-W output power. The amplifier is implemented in Qorvo's 90-nm T-gate GaN-on-SiC process. Each unit cell (UC) power amplifier is a three-stage, two-way power combined topology, with a layout shown in Fig. 3. Using nonlinear EEHEMT models for 2×40-, 4×30-, and 4×40-μm devices, drive staging is chosen with efficiency in mind. The bias conditions are kept at the modeled quiescent current, where 150 mA/mm corresponds to class-AB operation. The drain currents are 24, 36, and 48 mA for the first, second, and third stages, respectively.

Transistors in millimeter-wave processes have high gains in the lower frequency region, and therefore, stability must be carefully analyzed. Multiple stability analysis methods were performed during design—*K* factor, internal Nyquist stability, and loop gain [21], [22]. For in-band stability, resistors in the RF-path directly on the second stage gates introduce a small enough loss while maintaining overall efficiency. Small resistors, about 5 Ω, are in the dc path of the gates in all stages. To eliminate odd-mode instability, resistors are placed in the symmetry line and minimized in value using loop-gain simulations. The reactive output combiner is modeled and optimized to reduce current imbalances.

Due to the large lower frequency transistor gain, the out-of-band stability is considered under process variations, specifically with $g_m \pm 30\%$, $C_{gs} \mp 30\%$, and $C_{gd} \pm 30\%$ and the SiN thickness varied by $\pm 10\%$, which results in instabilities between 16 and 40 GHz. A small blocking capacitance (0.03 pF) absorbed in the matching network, together with low-frequency bypassed resistors, provides a viable solution for low-frequency gain reduction while maintaining bandwidth above 75 GHz. The resulting loop gain simulations of the final UC design in Fig. 4 show a phase margin greater than 30°.

The stabilized UC PAs are arranged, as shown in Fig. 2, where the input power is coupled to each of the five cascaded PAs for uniform drive. The outputs combine coherently, and each of the unit PAs operates under the same conditions (the

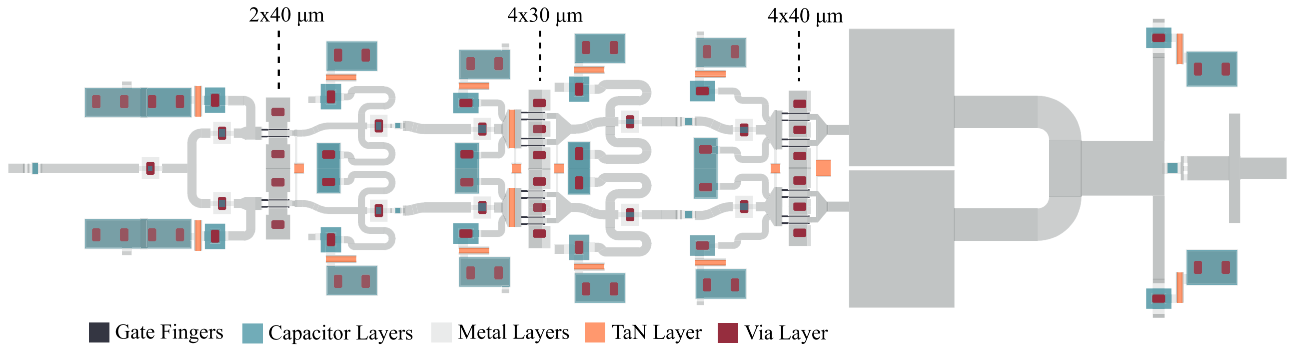

Fig. 3. Layout of a UC PA in the five-way chain power amplifier from Fig. 2. The staging ratio is 1:1.5:2, and the peripheries for stages 1, 2, and 3 are 160, 240, and 320 μm, respectively. The die area is 2.75×0.64 mm^2. Some metal layers and proprietary transistor layers have been removed.

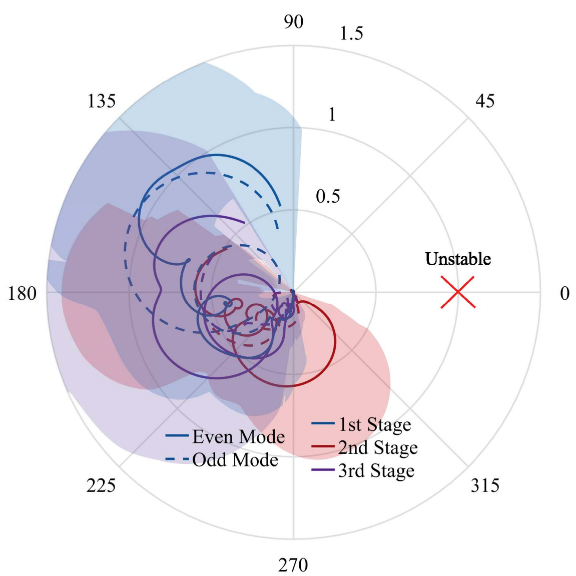

Fig. 4. Loop gain simulations from 0.1 to 120 GHz. Both even- and odd-mode (due to symmetry and two-way power combining) loop gains are analyzed at each stage. As can be seen, the nominal condition is far from the unstable region.

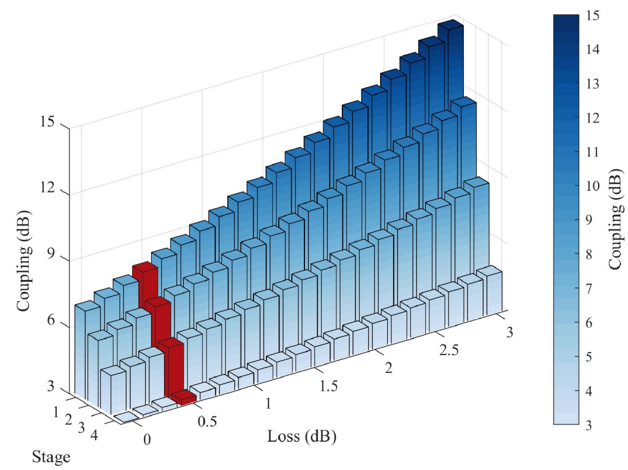

Fig. 5. Choice of coupling at each stage in Fig. 2 assuming 0.5 dB of loss in each coupler and subsequent transmission line is shown in red. A pragmatic approach would be to have this choice as a first pass and calculate the loss of each coupler design around the coupling value.

same gain, PAE, and P_{out}). A series of four Lange combiners with varying coupling coefficients are designed. The choice of the coupling factors C_1–C_4 is critical for equal power input, as described in [14]. For a five-way combiner, C_4 can be found from

$$C_4^2 = \frac{t_4^2}{1+t_4^2} \tag{1}$$

where t_4^2 is the efficiency of the fourth section. The remaining sections follow a recursive relationship:

$$C_i^2 = \frac{C_{i+1}^2 t_i^2}{1+C_{i+1}^2 t_i^2}, \qquad i = 3, 2, 1. \tag{2}$$

Fig. 5 shows the coupling coefficients for a five-stage chain PA, as a function of loss per stage. Equations (1) and (2) result in $(C_1, C_2, C_3, C_4) = (7.0, 6.0, 4.8, 3.0)$ dB, assuming an efficiency of 1. The ports of the Lange couplers require a layout with two 90° bends, modified from the standard layout, as shown in Fig. 6 for a 3-dB version. The coupler design is adjusted by adjusting the gap between the coupled lines. The different current distribution for the different port layouts is shown in Fig. 6. It can be seen that careful EM simulations result in a design with coupling and through parameters that are flat across the band.

In the final chain PA design from Fig. 2, the low-dispersion loss for each section (∼0.5 dB) is found through careful EM modeling with optimization of feed structures and minimized current crowding in the Lange fingers. This loss corresponds to the highlighted coupling coefficients in Fig. 5, which are implemented in the final layout shown in Fig. 7 of the fabricated MMIC.

The simulated and measured small-signal frequency response is shown in Fig. 8(a). The measured performance of two out of the 83 chips shows that the nonlinear model overestimates small-signal gain. Fig. 8(b) shows the simulated large-signal gain saturation across frequency. The simulated and measured large-signal performances, on the two MMICs, as a function of input power at 81 and 94 GHz are shown in Fig. 9(a) and (b), respectively. The small-signal measurements are obtained with an HP8510C network analyzer with millimeter-wave extenders. The SOLT calibration is performed at the GSG plane with an alumina *W*-band impedance standard substrate from Cascade Microtech. A power-calibrated scalar test setup is used for large-signal measurements. The signal is

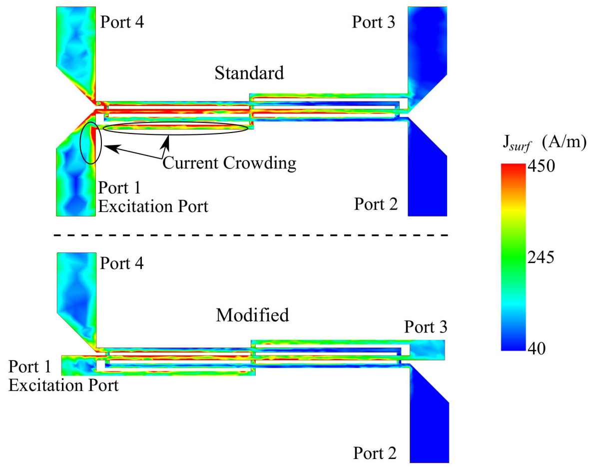

(a)

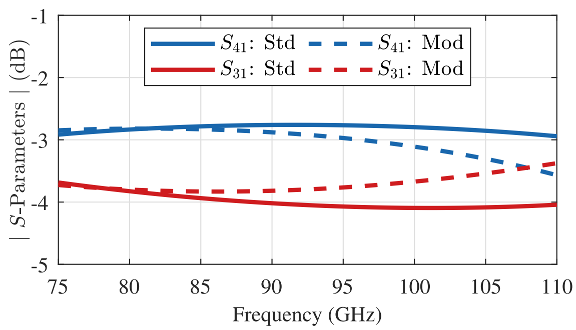

(b)

Fig. 6. (a) Standard W-band 3-dB Lange coupler port layout and modified layout as required by PA design showing surface current amplitude distribution. (b) Comparison of full-wave simulated through and coupled parameters for the two cases. The current distribution in the standard results in more variation across the band than the optimized design.

generated with a sweeper in Ka-band, followed by a Quinstar Ka-band amplifier, a passive tripler, and a W-band amplifier.

As shown in Fig. 7, 1- and 0.1-nF off-chip capacitors were mounted and are intended to suppress lower frequency bias-line oscillations. With the chip and capacitors mounted and under bias, no oscillations are seen on a 50-GHz spectrum analyzer connected via a 100-μm GSG-to-2.4 mm coax probe. Although a W-band spectrum analyzer was not available, our experience is that usually even higher frequency oscillations have downconverted frequency components that are observable with a spectrum analyzer, indicating that the PA is stable. In addition, the measurements are repeatable over time, and no fluctuations in the dc current are observed when biasing the device and with RF input power, which would provide another indication of instability.

Data across wafers were only available for small-signal parameters, and therefore, the remainder of this article uses small-signal data for the variation analysis. Nevertheless, this analysis can be easily extended to be statistically meaningful in the large-signal operation given large-signal measurements of the entire data set.

After fabrication, 83 chips from three separate wafers and two wafer lots were measured on-wafer in small-signal with

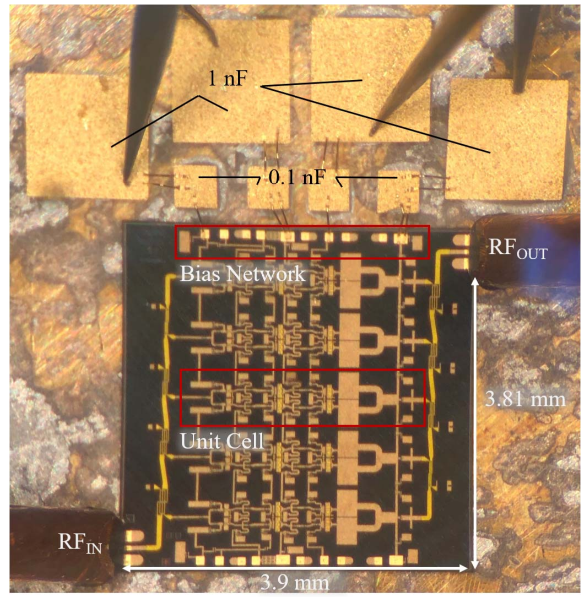

Fig. 7. Photograph of a five-way serially combined three-stage MMIC power amplifier designed for full W-band coverage mounted on a CuMo carrier with bondable MIM capacitors. The left GSG pad is the RF input, connected to coupler C_1. The size of the die is 3.9 mm × 3.81 mm.

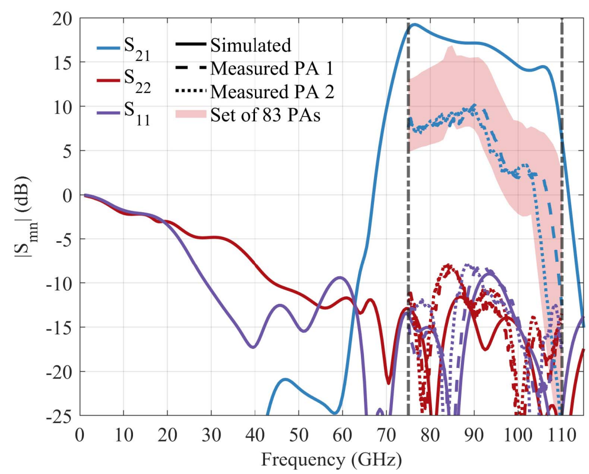

(a)

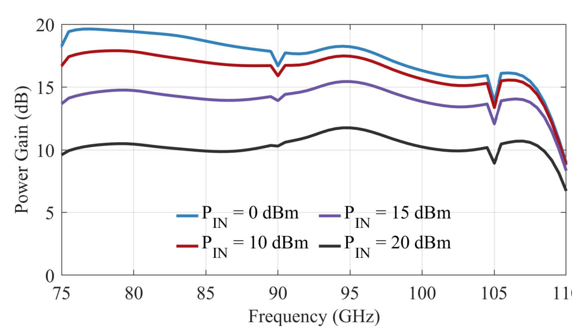

(b)

Fig. 8. (a) Small-signal simulated and measured performance of the five-section chain PA from 0.1 to 115 GHz with two representative mounted MMIC PAs. The red shaded area is the full range of the measured 83 MMICs. The dashed vertical bars represent the limitations of the measurement systems used. (b) Large-signal simulated gain shows similar compressive characteristics over frequency.

identical biasing conditions. The variation of S_{21} across the chips is shown in Fig. 10. The solid line is the mean value

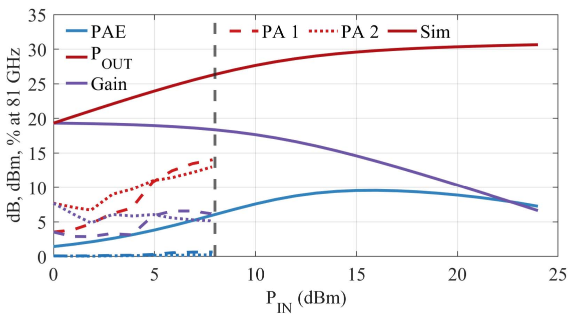

(a)

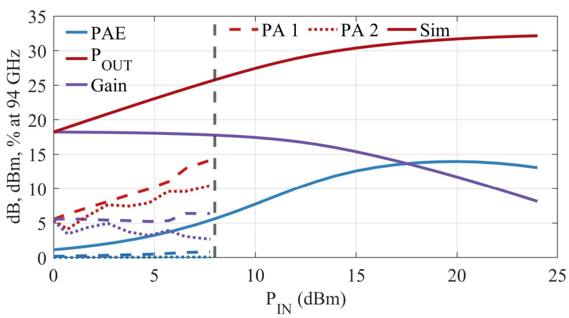

(b)

Fig. 9. Simulated and measured large-signal characteristics over a power input sweep at (a) 81 and (b) 94 GHz with two representative MMIC PAs. The dashed vertical bars represent the limitations of the measurement systems used.

of the measurements, and the shaded area encompasses two standard deviations. The two frequencies (81 and 94 GHz) are used in the remainder of this article for the statistical analysis.

With fabrication variation, each MMIC element has differing transmission amplitude and phase. If an array system designer is given 83 MMICs with an 4×4 array, there are $n!/(c!(n-c)!) = 83!/(16!(83-16)!) = 5 \times 10^{16}$ combinations without replacement. The goal of the remainder of this article is to estimate the effects of MMIC variation on the entire transmit array performance. The analysis method is universal and can be applied to each section of a dc-to-RF chain and is only dependent on performance data obtained from the measurement and/or simulation.

III. Statistical Analysis of Process Variation

The process variations for millimeter-wave MMICs with gates shorter than 100 nm are due to factors from epitaxial growth of GaN on SiC [23], [24] to gate definition [25], [26]. Substrate nonuniformities include warpage [27], [28], bowing [27], [29], and substrate and epilayer defects [24], [30]–[33]. Published knowledge on these defect effects on device performance is reviewed in [30], with increased leakage current, reduced blocking voltage, electric field crowding on surface pits, and local reduction of carrier lifetime being the most important contributors. One of the biggest sources of performance spread comes from poor process control in surface cleaning, which can cause variations in current collapse and the depletion region. All these mechanisms create large uncertainty of device performance from lot-to-lot, wafer-to-wafer, and across a wafer. Devices vary radially across a

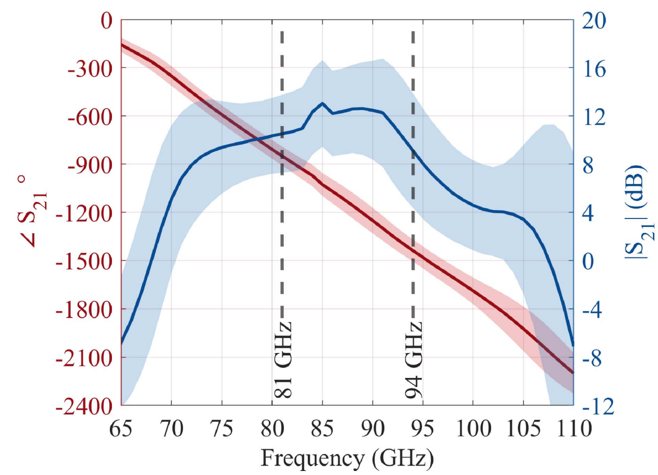

Fig. 10. Measured $|S_{21}|$ and unwrapped $\angle S_{21}$ for 83 MMIC PAs. The solid line is the mean, and the lightly shaded region is two standard deviations from the mean. The dashed lines are the frequencies with which the rest of this article uses in the analysis.

wafer due to bowing, ohmic contact and gate growth are affected by wafer warpage, and the epitaxial layer growth is sensitive to substrate defects. Table I summarizes qualitatively processing issues when transistors are scaled for millimeter-wave operation.

There are limited published statistical analyses for millimeter-wave power amplifier performance related to processing variations. A recent simple study that displays RF measured wafer statistics for K-band PA MMICs is given in [34] for a mature foundry process. The results show that even optimized commercial foundry processes have a significant variation in small- and large-signal regimes at lower millimeter-wave frequencies. For an analysis of device variations that can be applied to cascaded elements in a transmit array, the first step is to understand the pdf associated with the measured MMIC data.

Taking into account the complex fabrication parameter dependence from Table I, the full joint distribution function of the measured performance metrics can be perceived as a combination of dependent variables. Methods for analyzing amplitude and phase excitation errors in arrays assume Gaussian pdfs of errors, based on antenna fabrication tolerances [35], [36]. In [37], the Gaussian errors are assumed to be correlated in amplitude and phase, which changes the array gain pattern. However, the antenna array analyses do not take into account statistics related to the devices in the system chain. Here, we include a part of the transmit chain, including the MMIC PA and transitions from the MMIC to the antenna, which can then be combined with antenna element variations. In particular, we consider pdfs beyond simply Gaussians as a better description of the measured MMIC data.

A. Gaussian Bivariate Uncorrelated PDF

The following univariate Gaussian distribution is found from the mean, μ, and the variance, σ^2, of the measured data:

$$f\left(x|\mu,\sigma^2\right) = \frac{1}{\sigma\sqrt{2\pi}} e^{-\frac{1}{2}\left(\frac{x-\mu}{\sigma}\right)^2}. \quad (3)$$

TABLE I
SUMMARY OF mm-WAVE SCALING TRADEOFFS IN GaN HEMTs

Scale/Optimization	Improvement	Degradation
↓ gate length	↑ f_T	↑ short channel effects
↓ barrier thickness	↓ short channel effects	↑ gate leakage ↑ surface dispersion ↓ electron sheet density
↓ channel width (Length of source to drain)	↓ drain-to-source delay ↑ electron velocity ↑ max drain current	↑ parasitic capacitances ↓ breakdown voltage ↑ short channel effects
↑ passivation thickness	↑ device reliability ↓ surface dispersion	↑ parasitic capacitances
asymmetric gate	↑ breakdown voltage ↓ short channel effect ↓ gate current leakage	↓ yield
more complex ohmic contact	↓ R_{on} ↑ electron supply	↑ non-uniformity across wafer
back barrier	↑ electron confinement ↓ short channel effects	↑ deep traps

* References used in compilation of this table are [23], [25], [26], [32]

In the multivariate case, μ becomes a k-dimensional mean vector, and σ^2 becomes Σ, a $k \times k$ co-variance matrix, which, for the bivariate case, reduces to

$$\mu = \begin{pmatrix} \mu_X \\ \mu_Y \end{pmatrix}, \Sigma = \begin{pmatrix} \sigma_X^2 & \rho\sigma_X\sigma_Y \\ \rho\sigma_X\sigma_Y & \sigma_Y^2 \end{pmatrix}$$

where ρ is the correlation between x and y. In the example case discussed here, x is $|S_{21}|$, while y is $\angle S_{21}$, and X and Y represent samples. The relevant bivariate function that follows is then:

$$\begin{aligned} f(x, y|\mu, \Sigma) &= \frac{1}{2\pi\sigma_X\sigma_Y\sqrt{1-\rho^2}} \\ &\quad \times \exp\left(-\frac{1}{2(1-\rho^2)}\left[\frac{(x-\mu_X)^2}{\sigma_X^2} + \frac{(y-\mu_Y)^2}{\sigma_Y^2} \right.\right. \\ &\qquad \left.\left. - \frac{2\rho(x-\mu_X)(y-\mu_Y)}{\sigma_X\sigma_Y}\right]\right). \quad (4) \end{aligned}$$

The bivariate uncorrelated ($\rho = 0$) Gaussian for the sample data from Section II is visually represented in Fig. 11 at 81 and 94 GHz. There are large portions of the 2-D space that bivariate Gaussian estimation fails to describe accurately, even if the correlation is introduced. This, in turn, means that a statistical analysis of a transmit array will result in antenna complex coefficients with a skewed mean and, consequently, inaccurate predictions of the main beam and sidelobe variations due to MMIC variations.

B. Nonparametric Kernel Density Estimation

To describe the measured data set better, we investigate nonparametric pdfs. Here, we estimate the measured pdf using the kernel density estimator (KDE) [38]. To illustrate the difference from the Gaussian pdf, Fig. 12 compares a 1-D pdf for S_{21} at 81 and 94 GHz, showing that the Gaussian does not accurately capture univariate behavior. This exploratory data analysis reveals multimodal, asymmetric distributions with frequency-dispersive behavior.

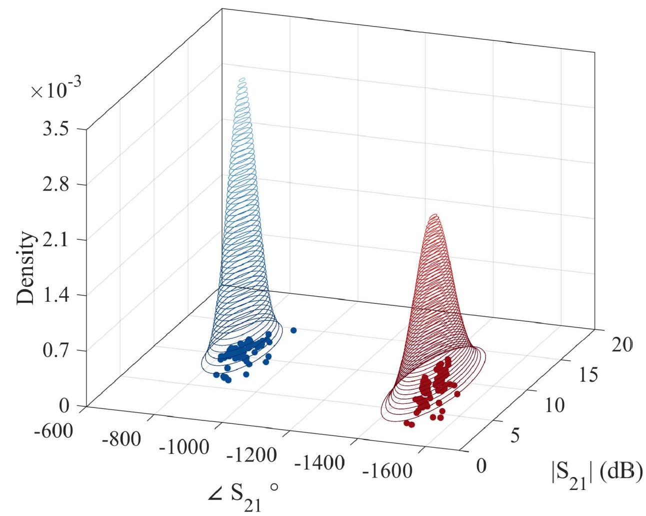

Fig. 11. Bivariate Gaussian distribution contours centered at the 1-D mean values with 1-D standard deviation values for both magnitude and phase of the measured MMICs at 81 (blue) and 94 GHz (red). The sample set at each frequency is scatter-plotted as well.

When dimensionality is increased, correlation can be maintained as follows. Let $\{X_1, Y_1\}, \ldots, \{X_{83}, Y_{83}\}$ be a 2-D vector sample from the measured data at a single frequency, with a pdf $f_d(x)$, where x has a general dimensionality of value d. The true univariate and bivariate densities can be estimated such that $\hat{f}_d(x)$ accurately approximates the marginal or joint distributions. The KDE is defined as

$$\hat{f}_d(x|H) = n^{-1}\sum_{i=1}^{n} K_H(x - X_i) \quad (5)$$

where K_H is a normalized continuous, unimodal, and symmetric kernel function. H is a symmetric, positive definite matrix of smoothing parameters, with dimension d, referred to as the bandwidth in this context. The kernel scales with H as follows:

$$K_H(x) = |H|^{-1/2}K\left(H^{-1/2}x\right) \quad (6)$$

where $|H|$ is applied to x and the kernel is normalized to this smoothing. The scaled kernels are then summed and normalized by the data set size n. For multivariate data sets, the Gaussian kernel is a popular choice. The scaled and translated version becomes

$$K_H(x - X_i) = (2\pi)^{-\frac{d}{2}}|H|^{-\frac{1}{2}}e^{-\frac{1}{2}(x-X_i)^T H^{-1}(x-X_i)} \quad (7)$$

which is centered at X_i and with variance matrix H, which needs to be determined when the pdf is unknown. One method to do this is unbiased cross validation (UCV), which is a "leave-one-out" cross-validation method where the estimated pdf is evaluated against an estimate of the same data minus one sample [39], [40]. The extended method of smoothed cross validation (SCV) has shown promise in reducing large variability in UCV by improving estimation of the integrated squared bias [41]. The multivariate extension of SCV has been explored by Duong [38]. This article uses an unconstrained

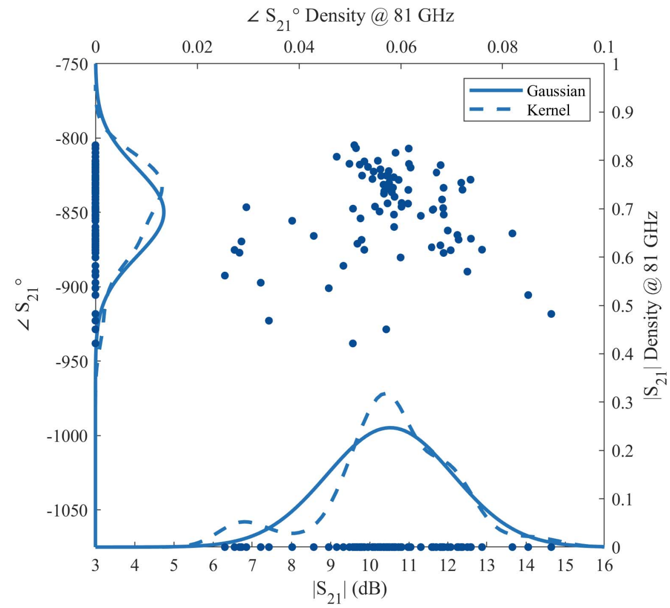

(a)

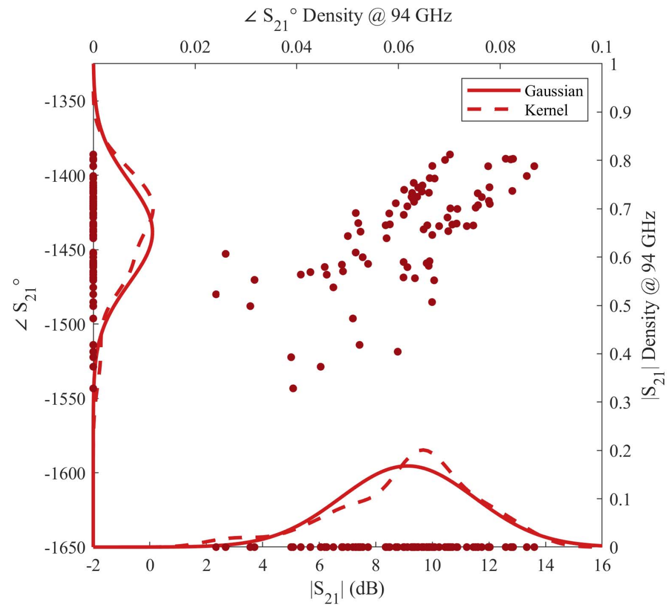

(b)

Fig. 12. For (a) 81 and (b) 94 GHz, the scatter plot shows the data set points. These are then shifted into a form of rug plot on each axis; here, both the Gaussian and the kernel density estimates are plotted in comparison. It is easy to see that the Gaussians do not accurately capture univariate densities.

SCV in 1-D, 2-D, and 4-D. Table II shows the values found for the univariate and bivariate cases $\hat{H}_{SCV}$, where f_1 is 81 GHz and f_2 is 94 GHz. Fig. 13 shows the result of the kernel density estimation applied to the measured MMIC data set for 81 and 94 GHz. A scatter of the 83 sample points is plotted on top of filled contours of the 2-D joint density estimate. The marginal density estimates are shown in the sides of the image. For an improved statistical analysis with an increased data set, standard sampling methods are applied, as described next for completeness.

TABLE II

UNCONSTRAINED SCV BANDWIDTH SELECTION

	Magnitude (1-D)	Phase (1-D)	Both (2-D)
f_1	$H_M = [0.45]$	$H_P = [10.17]$	$H_2 = \begin{bmatrix} 0.35 & -2.24 \\ -2.24 & 155.76 \end{bmatrix}$
f_2	$H_M = [0.72]$	$H_P = [11.76]$	$H_2 = \begin{bmatrix} 0.77 & 4.47 \\ 4.47 & 176.06 \end{bmatrix}$

IV. Markov Chain Monte Carlo Simulation

Markov chain Monte Carlo (MCMC) methods repeatedly sample a multidimensional continuous random variable from a target probability distribution $\pi(x)$. Ideally, these samples are independent and identically distributed (i.i.d.). Repeated MCMC i.i.d. sampling constructs a Markov chain with a distribution $\pi(x) = \hat{f}(x)$ determined by the kernel density estimates established in Section III. The aim of this KDE and MCMC combination is to create simulated data that can extend the analysis to include the MMIC package and antenna elements of a transmit array. The Metropolis–Hastings MCMC algorithm is used here, with details provided in Appendix A, in context with KDE.

MCMC methods have a few disadvantages that are specifically important for this analysis: 1) the draws are locally correlated and 2) the Markov chain needs significant simulation time to converge to the target distribution. The draws are correlated through the Markov process. Sets of nearby draws are correlated with each other and do not correctly reflect the target distribution, while over the long term the draws do. We choose a “jumping-width” of five draws with a single long chain to reduce autocorrelation and to reduce simulation time. Convergence means that the Markov chain has settled to the stationary distribution. The “burn-in” period of initial draws might follow a drastically different distribution and is typically discarded.

A result of this sampling algorithm for the 1-D cases with the first 1000 draws discarded can be seen in Fig. 14. The kernel density estimates of the original data set and the MCMC sample set show better agreement as the iterations of the MCMC are increased, allowing for a sufficient “tour” of the target density and tighter convergence.

The Metropolis–Hastings algorithm requires two initialization constraints: an arbitrary starting point and a proposal distribution. For simulations here, dependent symmetric univariate and bivariate Gaussian proposal densities are used, with variance found from the data set statistics, as seen in Section III-A. A proposal variance that is dependent on the original data set is found to have a positive effect on convergence time for individual dimensions and overall convergence.

With multivariate distributions, the algorithm requires a multidimensional initial point and multivariate joint proposal distribution of the same dimensions. The KDE is now evaluated across a N-dimensional (N-D) grid, and the acceptance ratio for the proposed N-D candidate states is calculated using N-D interpolation between meshed vertices. The benefit of a bivariate Metropolis–Hastings algorithm is apparent in

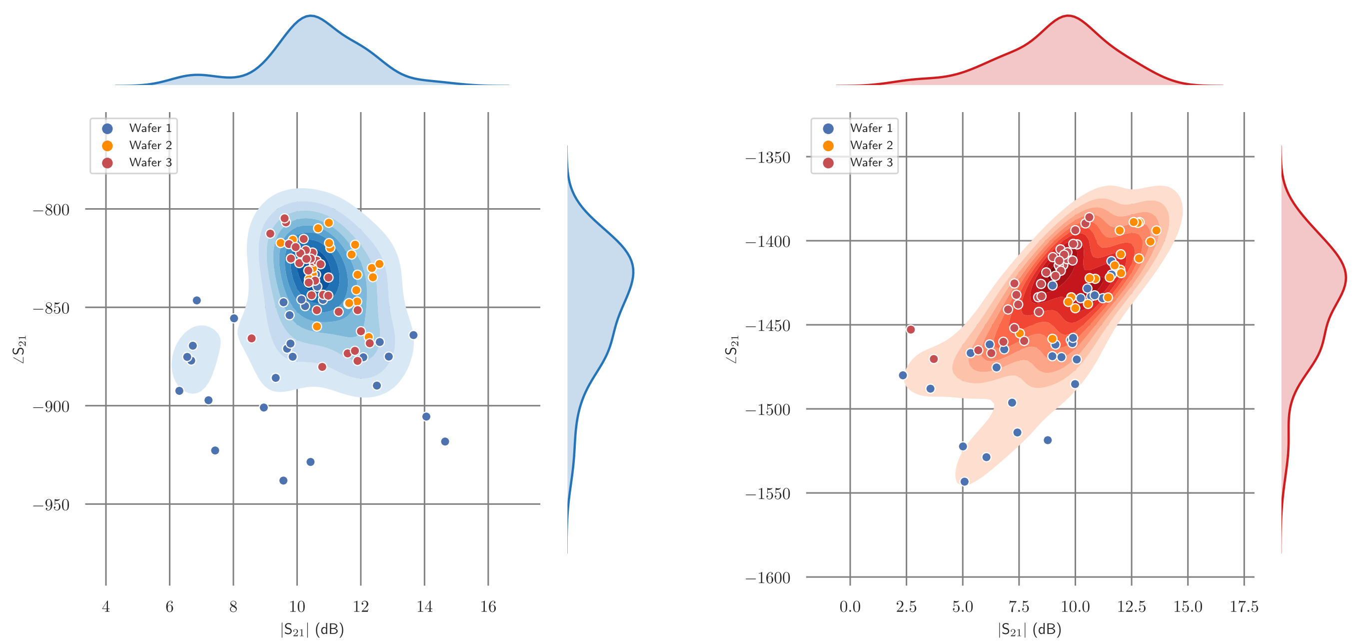

(a) (b)

Fig. 13. Univariate and bivariate kernel pdf estimates for small-signal gain of 83 measured MMICs from three wafers at (a) 81 and (b) 94 GHz. A conclusion that can be drawn is that wafer-to-wafer data can differ significantly. In this case, wafer 1 shows a larger variance than the other two.

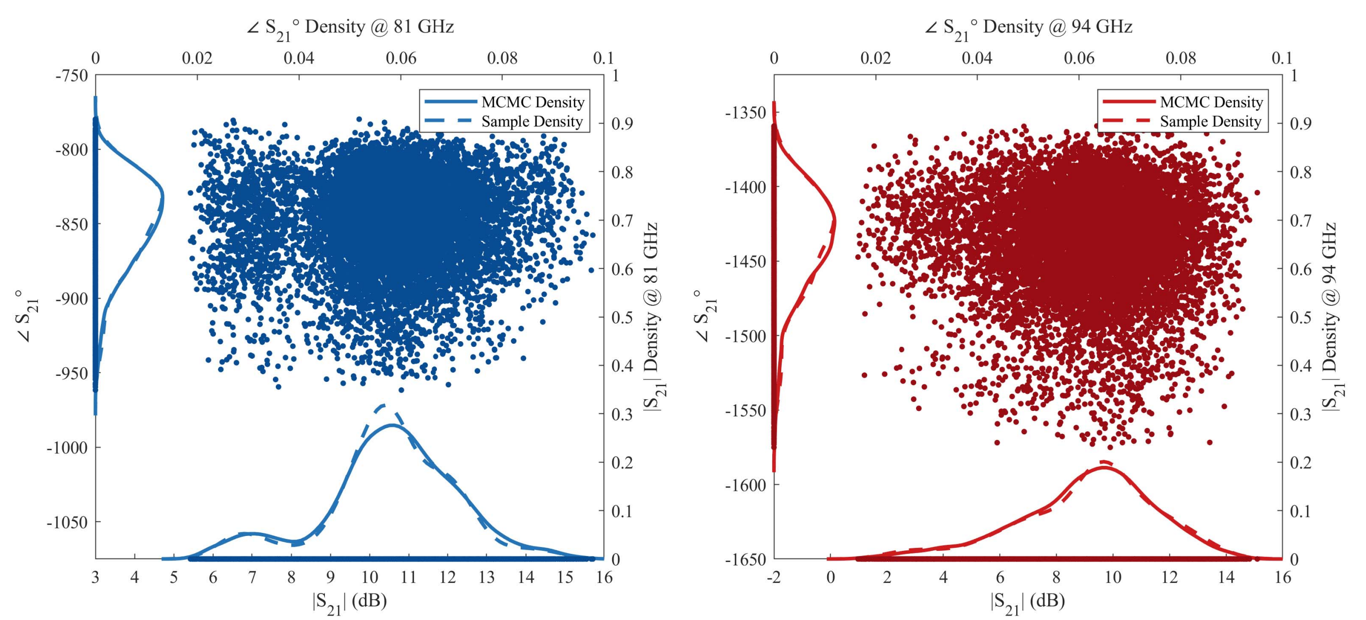

(a) (b)

Fig. 14. Univariate (magnitude and phase) MCMC draws are plotted at (a) 81 and (b) 94 GHz in scatter, underneath are the univariate kernel density estimates. The dashed lines are the data set kernel density estimates, as shown in Fig. 12, and the solid lines are the 1-D kernel density estimates of the MCMC results. Plotted are 10000 draws with the first 1000 draws discarded as a "burn-in" time.

Section III-B. The bivariate density maintains properties of dimensionality, such as parameter correlation, which would otherwise be removed by reducing to the univariate densities. This can be seen by a closer comparison of Figs. 14 and 15.

Another interesting comparison seen in Figs. 14 and 15 is the difference between the original data and MCMC samples when plotting the kernel density estimates of both. It has been shown that the MCMC rejection step introduces changes in the estimates of the bias and variance [42]. In the estimated pdf of the MCMC samples, regions can significantly deviate from the original data; and as such, this comparison does not necessarily show that the samples are drawn from the correct pdf. To identify that the MCMC has correctly drawn from the stationary distribution, Appendix B describes various metrics for convergence of the MCMC to the stationary distribution.

V. MMIC-Waveguide Transition Design

At this point, we have a good statistical representation of *W*-band MMIC PA gain variation across several wafers.

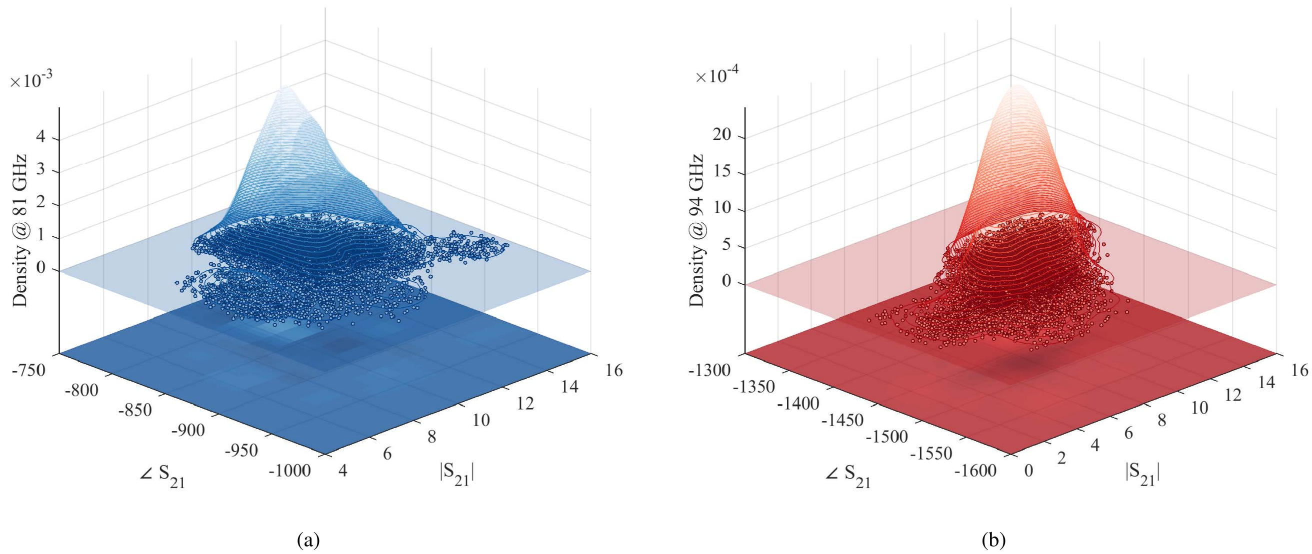

Fig. 15. Bivariate MCMC draws are plotted at (a) 81 and (b) 94 GHz in scatter underneath 3-D contour plots of the bivariate kernel density estimates. Underneath this 3-D plot is the relative error between the bivariate sample density estimate and the MCMC density estimate. The intensities of dark and light show spots where the MCMC either overestimated or underestimated, respectively. Of the simulation, 10 000 draws are plotted with the first 1000 draws discarded as a "burn-in" time.

The MMICs are next combined in a spatial power combining an array of waveguide horn antennas. The transition from each MMIC to a WR-10 rectangular waveguide is then analyzed with its fabrication- and mounting-related parameter spreads. A review of millimeter-wave waveguide transitions with various techniques is presented in [43]–[45], and the main designs of those references are conventional E-plane microstrip-to-waveguide transitions covering the entire W-band. The design implemented here is seen in the simulation model of Fig. 16. One wave-port excites the microstrip on the MMIC, while the other is the WR-10 waveguide in the split-block configuration seen in Fig. 1.

The transition is designed on a polished 100-μm Alumina substrate with top and bottom 5-μm-thick copper metal layers. On the top side, a rectangular probe radiates into the WR-10 cavity with a back short at $F = \lambda_g/4$, which is rounded due to CNC machining. A stepped-impedance microstrip line is used for matching from a capacitive load to a 50-Ω line on alumina that ends in a gold pad for a more reproducible bond-wire MMIC to transition interconnect. On the bottom side, the metal is not deposited underneath the rectangular probe and is only underneath the matching networks and 50-Ω line.

Using finite-element EM analysis in ANSYS HFSS, the nominal design shows less than 1 dB of insertion loss across W-band. However, a large amount of variability is introduced by fabrication and mounting. A linear parameter sweep covering six variable dimensions was performed; these are labeled in Fig. 16. In Fig. 16(a), A, B, C, D, and E correspond to the copper pedestal height underneath the MMIC, the bondwire height, the gap between MMIC and alumina, the typical tolerance of metallization (± 5 μm), and the placement in the waveguide, respectively. In Fig. 16(b), F is the back-short distance due to CNC machining tolerance. All these parameters have units of μm and do not vary more than 0.5 mm.

The result of the large parameter sweep on the transmission coefficient is seen in Fig. 17. The worst case transmission is up to -5 dB for the largest deviation in dimensions, with more sensitivity to C compared to other dimensions. The average value is centered around -3 dB with a standard deviation of about 1 dB. Lost in these Gaussian statistics, but seen in the regions of tightly spaced thin purple lines of Fig. 17, is that the transmission coefficient is not equally affected by the A–F dimension variations at all frequencies. This indicates that the transition analysis can also benefit from the density estimation and sampling presented in Sections III-B and IV.

VI. Cascaded S-Parameters in a Statistical Framework

Now, we have two separate cascaded statistically described networks: the amplifier S^a and the transition S^b. From [46], this cascaded network is a single two-port block, S^c, given by

$$\begin{bmatrix} S_{11}^c & S_{12}^c \\ S_{21}^c & S_{22}^c \end{bmatrix} = \begin{bmatrix} S_{11}^a + \kappa S_{12}^a S_{21}^a S_{11}^b & \kappa S_{12}^a S_{12}^b \\ \kappa S_{21}^a S_{21}^b & S_{22}^b + \kappa S_{12}^b S_{21}^b S_{22}^a \end{bmatrix}$$

where

$$\kappa = \frac{1}{1 - S_{22}^a S_{11}^b}. \tag{8}$$

It should be noted that S_{21}^c is a combination of four complex parameters (eight variables), two from each network. The bivariate S_{21}^a is estimated and sampled in Fig. 15 and Section IV. The other three complex parameters could be done in the same manner; however, separating these S-parameters would remove any within-network correlation structures.

The linear transition network, S^b, is physically symmetric and reciprocal; while creating the statistical data set, passivity under these assumptions is maintained. However, the amplifier matrix, S^a, has an unknown correlation between gain and output match, which affects the sampling. For each two-port

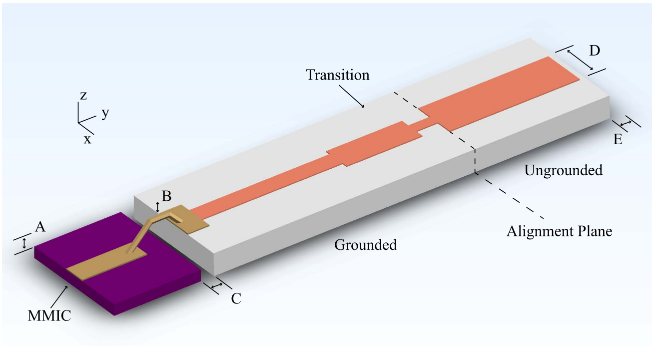

(a)

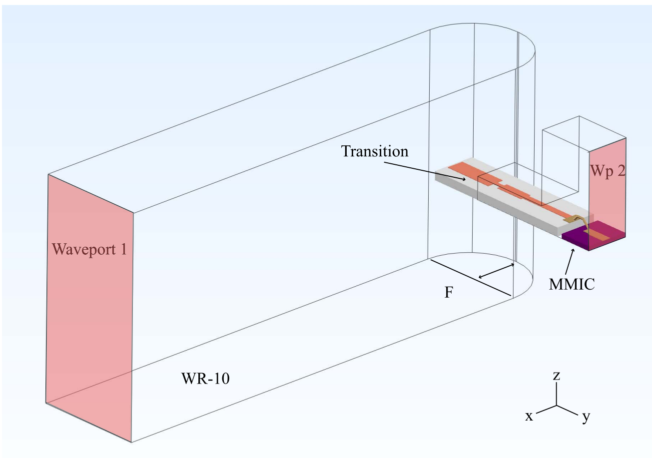

(b)

Fig. 16. *W*-band MMIC-to-waveguide transition, simulated in HFSS, consists of a copper-metalized alumina probe and a 25-μm gold bondwire. Six parameter sweeps are generated where in (a) A, B, C, D, and E correspond to copper pedestal height underneath the MMIC, bondwire height, the gap between MMIC and alumina, typical tolerance of metallization, and placement into the waveguide, respectively, and in (b) F is the backshort distance due to CNC machining tolerance.

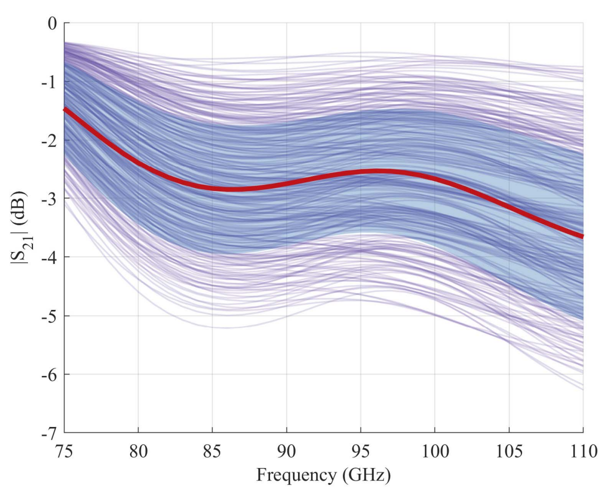

Fig. 17. Simulated parametric sweep of $|S_{21}|$ of the *W*-band transition, for dimensions [A, B, C, D, E, F] varied between [5:60 μm, 25:65 μm, 10:110 μm, -5:5 μm, -10:10 μm, 876:926 μm]. Plotted is the mean value in red, one standard deviation in blue fill, and all sweeps in thin transparent purple lines.

network, the interdependence of the S-parameters implies a cross correlation requiring a higher order model, which is an expansion of the bivariate to a multivariate distribution,

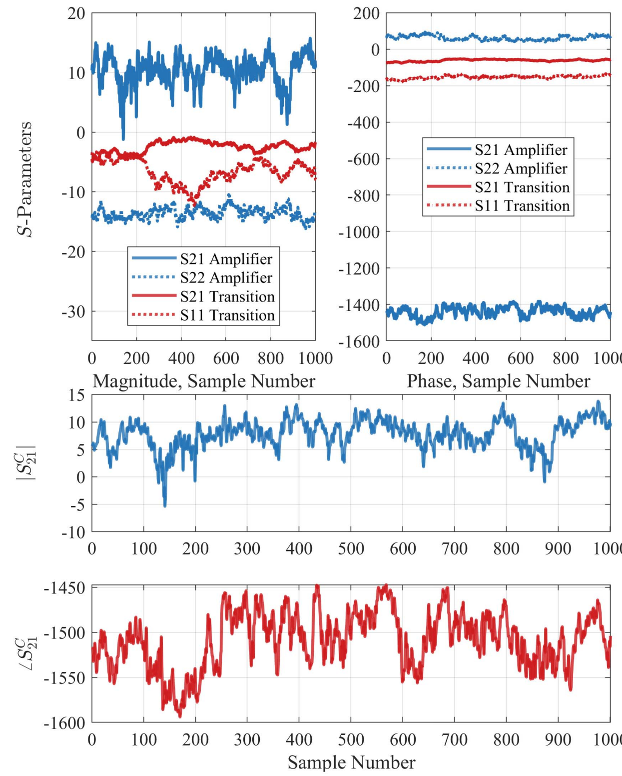

Fig. 18. Two separate simulated 4-D Markov chains for both the power amplifier and transition networks. The top-left plot is of the magnitude of the parameters, the top-right plot is of the wrapped phase of the parameters, and the bottom plot is of the cascaded network S^c_{21}.

in this case to four dimensions. The estimation and sampling algorithm is run once for each network, while the correlation between $[S^a_{21}, S^a_{22}]$ and $[S^b_{21}, S^b_{11}]$ is maintained. Random variables X for S^a and Y for S^b can be estimated and sampled in 4-D.

A resulting final cascaded S^c_{21} equation containing the two random variables, X and Y, where each sample point consists of four dimensions, is given by

$$Z_{S^c_{21}} = \frac{\left(X_{R(S^a_{21})} + iX_{I(S^a_{21})}\right)\left(Y_{R(S^b_{21})} + iY_{I(S^b_{21})}\right)}{1 - \left(X_{R(S^a_{22})} + iX_{I(S^a_{22})}\right)\left(Y_{R(S^b_{11})} + iY_{I(S^b_{11})}\right)}. \quad (9)$$

The resulting random variable Z is a complex parameter consisting of the same number of samples drawn from each MCMC chain. One such combination is presented in Fig. 18.

VII. Antenna Array Cascaded Statistics

A cascaded statistical description is next applied to a 16-element transmit antenna array. We use a 4×4 array as it is the smallest 2-D array that is used often as a subarray to validate performance and indicate potential scaling to a larger array. The block diagram showing relevant components is given in Fig. 19. The classical antenna array tolerance analysis, e.g., [35], [47], calculates the array factor based on random variations in amplitude and phase with a normal pdf and statistically independent errors. The array errors that are considered in these analyses are due to small variations in current excitations from the mechanical imprecision in

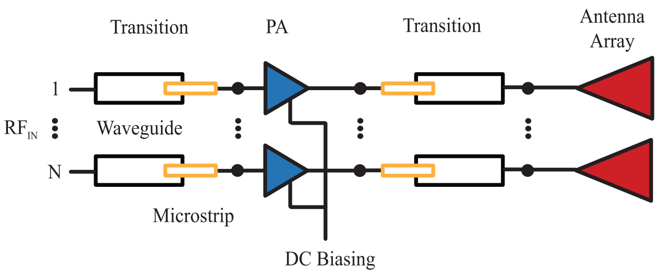

Fig. 19. Block diagram of the final transmit stage analyzed in Section VII.

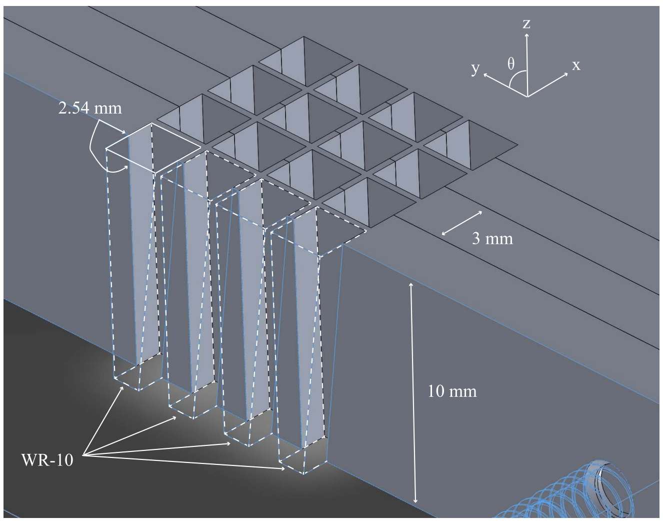

Fig. 20. 16-element horn array with detail of E-plane horn element. The element spacing is roughly 0.5 mm.

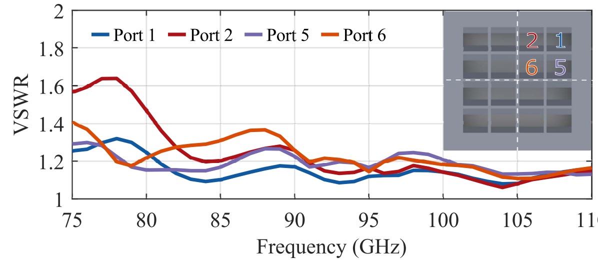

Fig. 21. Simulated VSWR of the horn antenna plotted over frequency.

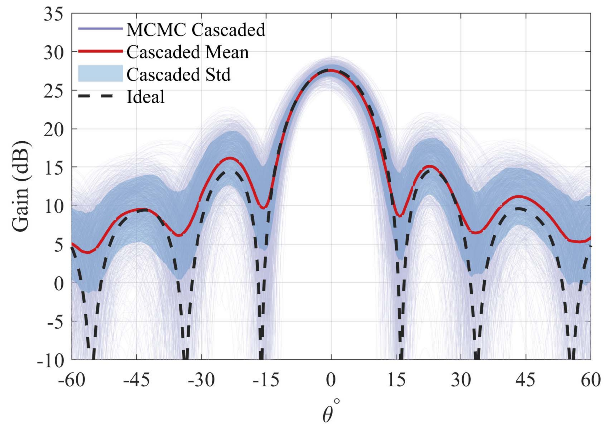

Fig. 22. Ideal radiation pattern of the array (dashed line), with cascaded statistical mean and standard deviation shown for comparison for broadside.

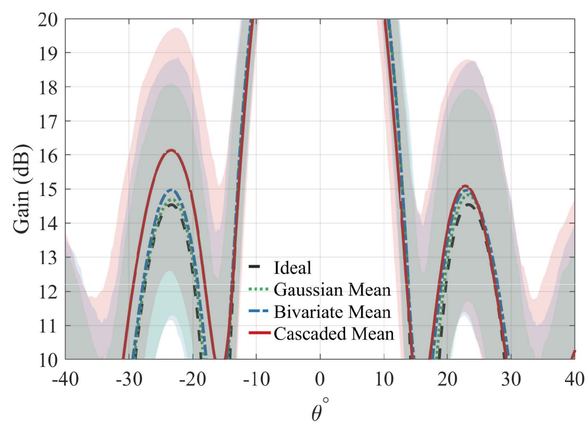

Fig. 23. Broadside gain comparison for an ideal antenna array excitation and the means of the various statistics. The overlapping shaded areas are the corresponding regions of one standard deviation.

the antenna elements. To extend to a multivariable analysis in 2-D arrays, Monte Carlo methods are proposed in [48]. Furthermore, the interval analysis that computes the bounds of a linear antenna array response by modeling bounds on the complex excitation is studied in [49] and [50]. In these works, 20-element and larger arrays are analyzed using ideal sources and isotropic antenna elements. Here, we extend the classical analysis to include measured PA variations.

The antenna element used as an example in the simulations is an E-plane square-aperture W-band horn fed by WR-10 waveguide feeds. The array, as shown in Fig. 20, is designed for fabrication with split-block machining in five parts stacked in the x-direction. The antenna array is simulated in Ansys HFSS. The simulated VSWR over the band for the four elements in each quadrant is shown in Fig. 21 when all elements are fed in-phase with equal amplitudes.

The array factor is classically given by

$$AF(u, v) = \sum_{m=1}^{M} \sum_{n=1}^{N} W_{mn} e^{j\phi_{mn}(u,v)} \tag{10}$$

but, in this case, the complex excitation W_{mn} is a statistical quantity that has the joint distribution, as estimated in Section VI, with $\hat{f}_d(x)$. This means that the radiation pattern of the array will also be a statistical quantity made of the cascaded samples of the MMIC and transition to waveguide, assuming that the antenna elements are ideal. It is computed by adding the independent far-field patterns from all 16 elements previously extracted from simulations. Using 1000 sets of 16 samples of the S_{21}^c cascaded vector, the descriptive statistics of the broadside pattern are shown in Figs. 22–24. The ideal array gain pattern is plotted in dashed black line, while all the 1000 Monte Carlo simulations are shown in thin purple lines with their mean shown in solid red. The shaded blue region represents one standard deviation away from the mean. Some conclusions from Fig. 22(a) are as follows: 1) the mean value of the sidelobe is about 1.5 dB higher than that of the ideal sidelobe level; 2) the increased value of the mean is not symmetrical; 3) the main beam is roughly at the same level as in the ideal case; and 4) the variance in the main lobe is smaller than in the sidelobes.

It is interesting to see the effects of different pdfs on the asymmetry in the sidelobe level for the broadside E-plane gain. Fig. 23 compares Gaussian, bivariate, and cascaded cases

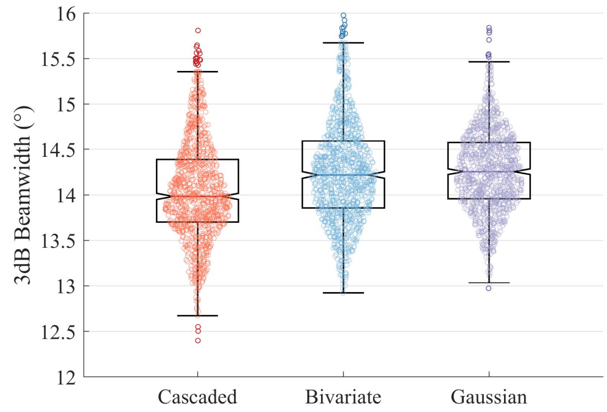

(a)

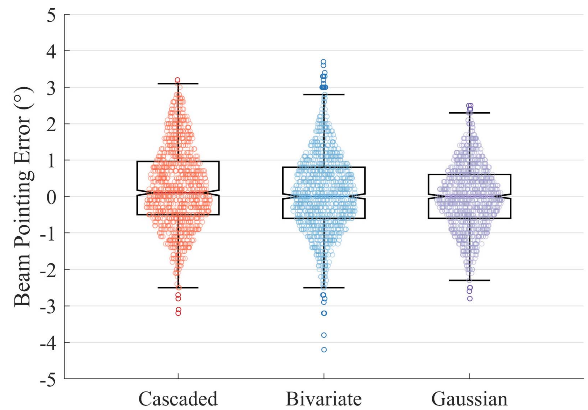

(b)

Fig. 24. For a comparison of the various statistics, boxplots with overlaid violin-plots are shown for (a) 3-dB beamwidth and (b) pointing error variation for the broadside.

from Sections III-A, III-B, and VI. For the Gaussian and bivariate cases, the nominal value of the alumina transition is used. In the Gaussian case, the mean performs close to ideal and affects the main beam and sidelobes equally. The bivariate KDE samples show similar behavior, but with slightly higher values. However, the cascaded draws result in an asymmetry, where one sidelobe is around the same as the bivariate case, while the other is 1.5 dB higher.

Using the main beam deviations for a broadside E-plane cut, the 3-dB beamwidth is investigated in Fig. 24(a). The median value of the cascaded is roughly 0.3° smaller than the bivariate and Gaussian cases. The cascaded set shows a large positive skew, with the majority of 3-dB beamwidths are smaller and below 14°. The bivariate case shows a larger interquartile range (width of the boxed region) than the Gaussian, with a slightly lower median and a slight positive skew toward the smaller beamwidth.

In Fig. 24(b), the beam pointing error is calculated as the difference between the maximum values of the ideal case and the various pdfs. Interestingly, the cascaded case shows a preference for a specific direction, and the median is centered around 0.1°. This positive skew can be seen as well in the colored violin plots. In the bivariate case, the median is centered at 0°; however, the interquartile range is larger than for the Gaussian and appears to have more outliers that extend beyond 3° of beam pointing error. For both boxplot images [see Fig. 24(a) and (b)], the Whisker maximum and minimum are set to a default of 1.5 interquartile range.

The analysis shows that an accurate prediction of antenna radiation pattern characteristics requires taking into account the statistical dispersion of the amplifiers and transitions, especially at the W-band where process-related variations can be high. For a 16-element spatial power combining array, the first sidelobe level can vary ±6 dB and the EIRP by ±3 dB when random amplifier chips from the measured batch are chosen to populate the array.

VIII. Conclusion

This article presents statistical analysis for a spatial power combining array that operates across the W-band. The analysis starts from measured on-wafer S-parameters for about 80 power-combined amplifier chips designed in an experimental 90-nm GaN on SiC process. The pdfs, both parametric (Gaussian) and nonparametric (kernel density estimation), are generated from measured data and propagated using a Markov chain Monte Carlo to the antenna elements. The connection from the chips to alumina microstrip-to-waveguide transitions is analyzed with full-wave simulations in conjunction with the same statistical approach. The analysis is given on cases of the small-signal MMIC gain cascaded with passive transitions with a simple Gaussian model, a bivariate kernel density estimated model, and a model developed by using multivariate S-parameters as complex random variables in a cascaded network. The waveguides feed a 16-element square horn array, and the effect of cascaded statistics on EIRP is quantified. An extension to cascaded antenna fabrication tolerances is straightforward and follows the same methodology.

Furthermore, the knowledge of process variations and their correlated statistics can give an insight into the ability to calibrate a phased array without pretesting and choosing MMICs, as has been done in many millimeter-wave transmit arrays. Calibration techniques require a high degree of phase and amplitude accuracy in the beamformer for acceptable calibration resolution, as can be seen in examples of narrowband arrays at Ku-band (17.3–17.8 GHz) [51], relatively broadband Ka-band arrays (37–42 GHz) [52], and a 90.7-GHz 384-element array [53]. Advance knowledge of the gain amplitude and phase can inform the decision related to costly preselection of MMICs or the need for bias control across the transmit array. Improving the error on gain amplitude is especially important for narrowband transmit arrays, where bias control affects the efficiency and contributes to the reduction in EIRP and increase in thermal stress. In broadband arrays, the phase variations in calibration become more critical, as does element-to-element coupling and active scan coefficient that takes into account variations in large-signal PA parameters.

Appendix A
Metropolis–Hastings Algorithm

The Metropolis–Hastings algorithm is used here for the estimation and sampling by creating a Markov chain through a

Algorithm 1: Univariate Metropolis–Hastings

Data: A kernel-density estimated uni-variate density $\hat{f}(x)$

Result: Markov chain of unique independent and identically distributed draws as X

Initialize:

Choose proposal density $\sim q(x)$

Choose an arbitrary point x_0^i

for *iterations = 1,2...N* **do**

  Propose: $x^{\text{cand}} \sim q(x^i|x^{i-1})$

  Acceptance probability:

  $\alpha(x^{\text{cand}}|x^{i-1}) = min\{1, \frac{q(x^{i-1}|x^{\text{cand}})}{q(x^{\text{cand}}|x^{i-1})} \frac{\hat{f}(x^{\text{cand}})}{\hat{f}(x^{i-1})}\}$

  $u \sim Unif(0, 1)$

  if $u < \alpha$ **then**

    Accept: $x^i = x^{\text{cand}}$

    Set: $X(i) = x^i$

  else

    Reject: $x^i = x^{i-1}$

  end

end

series of accept–reject steps, as described in Algorithm 1 [54]. This algorithm randomly attempts movements in the parameter space, occasionally accepting moves or lingering in the same state. The acceptance ratio α demonstrates how probable the newly proposed state is in relation to the current state, with respect to the target distribution. Movements that are more probable than the current state will consistently be accepted. However, if a movement is less probable, a rejection might occur, and as the relative drop in probability increases, the proposed state is rejected with a higher likelihood.

A common choice for the proposal distribution is a symmetric distribution $q(x^i|x^{i-1}) = q(x^{i-1}|x^i)$. Some standard symmetric proposals are Gaussian or uniform distributions centered at the chain's current state. The symmetry cancels out the effects of the proposal density, resulting in an acceptance ratio $\alpha(x^{\text{cand}}|x^{i-1})$ that is proportional to how likely the current state, x^{i-1}, and the proposed state x^{cand} are under the full joint density distribution. As the number of dimensions increases in the target density, the proposal acceptances need to be optimal for all dimensions simultaneously to avoid excessively slow convergence.

Appendix B
MCMC Convergence

There are different ways to test for MCMC convergence. Trace plots can show if the parameters are "mixing" well, defined as moving around the parameter space efficiently. Alternatively, autocorrelation on the Markov chains should display a drop in magnitude as the lag increases. These can show potential for convergence of a single chain but do not produce rigorous criteria for determining convergence for an estimated pdf.

Gelman and Rubin [55] created a convergence metric that looks at inferences from m simulated Markov chains and

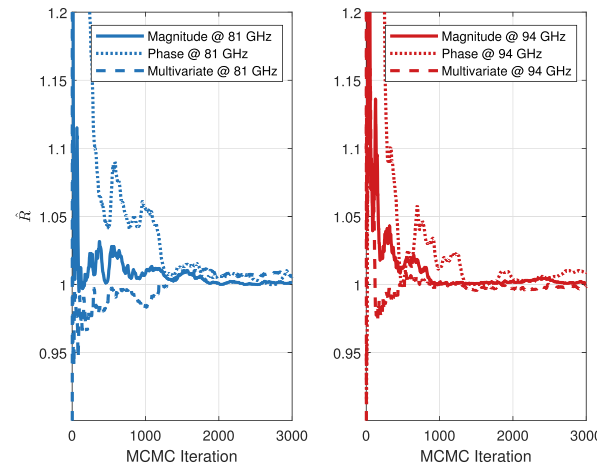

Fig. 25. Gelman and Rubin's diagnostic of potential scale reduction factor as it changes through the MCMC iterations. Ideally, the chains converge to 1; after reaching below a certain threshold for $\hat{R}$, typically, it is said to be converged. This metric relays a solid value for "burn-in" time; approximately, here, it would be 1000 draws.

compares these to inferences made by combining n draws from all sequences. To do this, the average of the m within-sequence variances is initially calculated as

$$W = \frac{1}{m(n-1)} \sum_{j=1}^{m} \sum_{t=1}^{n} (\theta_{jt} - \bar{\theta}_{j.})^2 \tag{11}$$

where θ_{jt} is the sample point, and $\bar{\theta}_{j.}$ is the average over the draws (t). The variance B/n between the m sequence means is calculated as

$$\frac{B}{n} = \frac{1}{m-1} \sum_{j=1}^{m} (\bar{\theta}_{j.} - \bar{\theta}_{..})^2 \tag{12}$$

where $\bar{\theta}_{..}$ is the average over the entire set of chains. Then, an estimate of the variance of the stationary distribution as a weighted average of W and B is formed

$$\hat{\sigma}^2 = \frac{n-1}{n} W + \frac{B}{n}. \tag{13}$$

Finally, the potential scale reduction factor ($\hat{R}$) is calculated as

$$\hat{R} = \sqrt{\frac{(m+1)}{m} \frac{\hat{\sigma}^2}{W} - \frac{n-1}{mn}} \tag{14}$$

which reduces to 1 as $n \to \infty$. A large $\hat{R}$ suggests that either the estimate of the variance $\hat{\sigma}^2$ can be further decreased by more simulations or that further simulation will increase W since the simulated chains have not made a full route of the target distribution. On the other hand, if $\hat{R}$ is close to 1, it can be concluded that each of the m sets of n simulated observations is close to the target distribution.

An extended metric for the multivariate case can be found in [56]. W and B/n denote within- and between-sequence covariance estimate matrices in d dimensions, respectively. $\hat{V}$ becomes the estimate of the posterior variance–covariance matrix, and $\hat{R}$, the multivariate $\hat{R}$, is determined as a scalar measure of the distance between $\hat{V}$ and W. Fig. 25 shows $\hat{R}$ as a function of the chain iteration for the amplitude and phase of the MMIC gain at 81 and 94 GHz, as well as the univariate, bivariate, and 4-D cases (as needed in Section VI). $\hat{R}$ quickly drops to 1 for all parameters, and it can be concluded that m chains are each close to the target distribution. A burn-in time is set as a threshold; when $\hat{R}$ is below this threshold, the draws can be taken as i.i.d.

Acknowledgment

The authors would like to thank Qorvo for the help in RF data acquisition, especially Dr. Shuoqi Chen and Dr. Yu Cao. They would also like to thank Aman Samaiyar, Michael Grayson, and Prof. Jem Corcoran for helpful discussions regarding this analysis method.

References

[1] S. Sun, T. S. Rappaport, M. Shafi, P. Tang, J. Zhang, and P. J. Smith, "Propagation models and performance evaluation for 5G millimeter-wave bands," *IEEE Trans. Veh. Technol.*, vol. 67, no. 9, pp. 8422–8439, Sep. 2018.

[2] P. M. Asbeck, N. Rostomyan, M. Ozen, B. Rabet, and J. A. Jayamon, "Power amplifiers for mm-wave 5G applications: Technology comparisons and CMOS-SOI demonstration circuits," *IEEE Trans. Microw. Theory Techn.*, vol. 67, no. 7, pp. 3099–3109, Jul. 2019.

[3] K. Brown *et al.*, "Ultra-compact high speed mmW transceiver using GaN power amplifier technology," in *IEEE MTT-S Int. Microw. Symp. Dig.*, May 2015, pp. 1–3.

[4] F. Boes *et al.*, "Multi-gigabit e-band wireless data transmission," in *IEEE MTT-S Int. Microw. Symp. Dig.*, May 2015, pp. 1–4.

[5] X. Gu, A. Valdes-Garcia, A. Natarajan, B. Sadhu, D. Liu, and S. K. Reynolds, "*W*-Band scalable phased arrays for imaging and communications," *IEEE Commun. Mag.*, vol. 53, no. 4, pp. 196–204, Apr. 2015.

[6] B.-H. Ku *et al.*, "A 77–81-GHz 16-element phased-array receiver with $\pm 50^\circ$ beam scanning for advanced automotive radars," *IEEE Trans. Microw. Theory Techn.*, vol. 62, no. 11, pp. 2823–2832, Nov. 2014.

[7] P. Schmalenberg, J. S. Lee, and K. Shiozaki, "A sige-based 16-channel phased array radar system at *W*-Band for automotive applications," in *Proc. Eur. Radar Conf.*, Oct. 2013, pp. 299–302.

[8] D. Bleh *et al.*, "A 100 GHz FMCW MIMO radar system for 3D image reconstruction," in *Proc. 13th Eur. Radar Conf. (EuRAD)*, Oct. 2016, pp. 37–40.

[9] K. Brown *et al.*, "7kW GaN *W*-Band transmitter," in *IEEE MTT-S Int. Microw. Symp. Dig.*, May 2016, pp. 1–3.

[10] J. J. Sowers *et al.*, "A 36 W, V-band, solid state source," in *IEEE MTT-S Int. Microw. Symp. Dig.*, Jun. 1999, pp. 235–238.

[11] A. Agrawal and A. Jablon, "A calibration technique for active phased array antennas," in *Proc. IEEE Int. Symp. Phased Array Syst. Technol.*, Oct. 2003, pp. 223–228.

[12] C. Fulton, J. Salazar, D. Zrnic, D. Mirkovic, I. Ivic, and D. Doviak, "Polarimetrie phased array calibration for large-scale multi-mission radar applications," in *Proc. IEEE Radar Conf. (RadarConf)*, Apr. 2018, pp. 1272–1277.

[13] S. D. Silverstein, "Application of orthogonal codes to the calibration of active phased array antennas for communication satellites," *IEEE Trans. Signal Process.*, vol. 45, no. 1, pp. 206–218, 1997.

[14] J. Schellenberg, B. Kim, and T. Phan, "*W*-Band, broadband 2w GaN MMIC," in *IEEE MTT-S Int. Microw. Symp. Dig.*, Jun. 2013, pp. 1–4.

[15] A. Margomenos *et al.*, "Gan technology for e, w and G-band applications," in *Proc. IEEE Compound Semiconductor Integr. Circuit Symp. (CSICS)*, Oct. 2014, pp. 1–4.

[16] S. Chen, L. Witkowski, and X. Gu, "(Invited) important recent advancement of GaN technology and MMICs for *W*-Band applications," *ECS Trans.*, vol. 80, no. 10, pp. 945–952, Oct. 2017.

[17] M. van Heijningen *et al.*, "*W*-Band power amplifier MMIC with 400 mw output power in 0.1 μm AlGaN/GaN technology," in *Proc. 7th Eur. Microw. Integr. Circuit Conf.*, 2012, pp. 135–138.

[18] Y. Niida *et al.*, "3.6 W/mm high power density *W*-Band InAlGaN/GaN HEMT MMIC power amplifier," in *Proc. IEEE Topical Conf. Power Model. Wireless Radio Appl. (PAWR)*, Jan. 2016, pp. 24–26.

[19] A. Brown, K. Brown, J. Chen, K. C. Hwang, N. Kolias, and R. Scott, "*W*-Band GaN power amplifier MMICs," in *IEEE MTT-S Int. Microw. Symp. Dig.*, Jun. 2011, pp. 1–4.

[20] M. Pinto, "Millimeter-wave GAN solid-state arrays," Ph.D. dissertation, Dept. Elect., Comput., Energy Eng., Univ. Colorado Boulder, Boulder, CO, USA, 2019.

[21] C. Campbell, "Microwave monolithic power amplifier design," in *Wiley Encyclopedia of Electrical and Electronics Engineering*, J. G. Webster, Ed. Hoboken, NJ, USA: Wiley, 2013.

[22] A. Suarez, "Check the stability: Stability analysis methods for microwave circuits," *IEEE Microw. Mag.*, vol. 16, no. 5, pp. 69–90, Jun. 2015.

[23] Q. Rudiger, *GaN Electronics*. Berlin, Germany: Springer, 2007.

[24] H. Tsuchida, I. Kamata, T. Miyazawa, M. Ito, X. Zhang, and M. Nagano, "Recent advances in 4H-SiC epitaxy for high-voltage power devices," *Mater. Sci. Semicond. Process.*, vol. 78, pp. 2–12, May 2018.

[25] P. Waltereit *et al.*, "GaN HEMT and MMIC development at fraunhofer IAF: Performance and reliability," *Phys. Status Solidi (A)*, vol. 206, no. 6, pp. 1215–1220, Jun. 2009.

[26] K. Shinohara *et al.*, "Scaling of GaN HEMTs and Schottky diodes for submillimeter-wave MMIC applications," *IEEE Trans. Electron Devices*, vol. 60, no. 10, pp. 2982–2996, Oct. 2013.

[27] A. Ellison *et al.*, "Wafer warpage, crystal bending and interface properties of 4H-SiC epi-wafers," *Diamond Rel. Mater.*, vol. 6, no. 10, pp. 1369–1373, Aug. 1997.

[28] Y. Ohno and M. Kuzuhara, "Application of GaN-based heterojunction FETs for advanced wireless communication," *IEEE Trans. Electron Devices*, vol. 48, no. 3, pp. 517–523, Mar. 2001.

[29] M. Treu, R. Rupp, P. Blaschitz, and J. Hilsenbeck, "Commercial sic device processing: Status and requirements with respect to sic based power devices," *Superlattices Microstruct.*, vol. 40, no. 4, pp. 380–387, 2006.

[30] T. Kimoto, "Material science and device physics in SiC technology for high-voltage power devices," *Jpn. J. Appl. Phys.*, vol. 54, no. 4, Mar. 2015, Art. no. 040103.

[31] H. Jacobson *et al.*, "Dislocation evolution in 4h-sic epitaxial layers," *J. Appl. Phys.*, vol. 91, no. 10, pp. 6354–6360, 2002.

[32] T. Ohno, H. Yamaguchi, S. Kuroda, K. Kojima, T. Suzuki, and K. Arai, "Direct observation of dislocations propagated from 4H–SiC substrate to epitaxial layer by X-ray topography," *J. Cryst. Growth*, vol. 260, nos. 1–2, pp. 209–216, Jan. 2004.

[33] A. C. Lang, J. L. Hart, J. G. Wen, D. J. Miller, D. J. Meyer, and M. L. Taheri, "I2 basal stacking fault as a degradation mechanism in reverse gate-biased AlGaN/GaN HEMTs," *Appl. Phys. Lett.*, vol. 109, no. 13, Sep. 2016, Art. no. 133509.

[34] M. R. Duffy, G. Lasser, G. Nevett, M. Roberg, and Z. Popovic, "A three-stage 18.5–24-GHz GaN-on-SiC 4 w 40% efficient MMIC PA," *IEEE J. Solid-State Circuits*, vol. 54, no. 9, pp. 2402–2410, Sep. 2019.

[35] J. Ruze, "Antenna tolerance theory—A review," *Proc. IEEE*, vol. 54, no. 4, pp. 633–640, Apr. 1966.

[36] J. Howard, "Statistical patterns of a general array," *IEEE Trans. Antennas Propag.*, vol. AP-15, no. 1, pp. 60–65, Jan. 1967.

[37] A. J. van den Biggelaar, U. Johannsen, P. Mattheijssen, and A. B. Smolders, "Improved statistical model on the effect of random errors in the phase and amplitude of element excitations on the array radiation pattern," *IEEE Trans. Antennas Propag.*, vol. 66, no. 5, pp. 2309–2317, May 2018.

[38] J. E. Chacon and T. Duong, "Multivariate Kernel smoothing and its applications," in *Chapman & Hall/CRC Monographs on Statistics & Applied Probability*. London, U.K.: Chapman & Hall, 2018.

[39] M. Rudemo, "Empirical choice of histograms and kernel density estimators," *Scandin. J. Statist.*, vol. 9, no. 2, pp. 65–78, 1982.

[40] A. Bowman and A. Azzalini, "Applied smoothing techniques for data analysis: The Kernel approach with S-plus illustrations," in *Oxford Statistical Science Series*. Oxford, U.K.: OUP Oxford, 1997.

[41] P. Hall, J. Marron, and B. Park, "Smoothed cross-validation," *Probab. Theory Rel. Fields*, vol. 92, no. 1, pp. 1–20, Mar. 1992.

[42] M. Skold and G. O. Roberts, "Density estimation for the metropolis-hastings algorithm," *Scandin. J. Statist.*, vol. 30, no. 4, pp. 699–718, Dec. 2003.

[43] E. S. Li, G.-X. Tong, and D. C. Niu, "Full *W*-Band waveguide-to-microstrip transition with new E-plane probe," *IEEE Microw. Wireless Compon. Lett.*, vol. 23, no. 1, pp. 4–6, Jan. 2013.

[44] J. Doo, W. Park, W. Choe, and J. Jeong, "Design of broadband *W*-Band waveguide package and application to low noise amplifier module," *Electronics*, vol. 8, no. 5, p. 523, May 2019.

[45] A. U. Zaman, V. Vassilev, P.-S. Kildal, and H. Zirath, "Millimeter wave E-Plane transition from waveguide to microstrip line with large substrate size related to MMIC integration," *IEEE Microw. Wireless Compon. Lett.*, vol. 26, no. 7, pp. 481–483, Jul. 2016.

[46] F. Gardiol, "Microstrip Circuits," in *Wiley Series in Microwave and Optical Engineering*. Hoboken, NJ, USA: Wiley, 1994.

[47] J. K. Hsiao, "Design of error tolerance of a phased array," *Electron. Lett.*, vol. 21, no. 19, pp. 834–836, Sep. 1985.

[48] J. Lee, Y. Lee, and H. Kim, "Decision of error tolerance in array element by the Monte Carlo method," *IEEE Trans. Antennas Propag.*, vol. 53, no. 4, pp. 1325–1331, Apr. 2005.

[49] L. Poli, P. Rocca, N. Anselmi, and A. Massa, "Dealing with uncertainties on phase weighting of linear antenna arrays by means of interval-based tolerance analysis," *IEEE Trans. Antennas Propag.*, vol. 63, no. 7, pp. 3229–3234, Jul. 2015.

[50] N. Anselmi, L. Manica, P. Rocca, and A. Massa, "Tolerance analysis of antenna arrays through interval arithmetic," *IEEE Trans. Antennas Propag.*, vol. 61, no. 11, pp. 5496–5507, Nov. 2013.

[51] E. Lier, M. Zemlyansky, D. Purdy, and D. Farina, "Phased array calibration and characterization based on orthogonal coding: Theory and experimental validation," in *Proc. IEEE Int. Symp. Phased Array Syst. Technol.*, Oct. 2010, pp. 271–278.

[52] Y. Yin *et al.*, "A 37–42-GHz 8 × 8 phased-array with 48–51-dBm EIRP, 64–QAM 30-Gb/s data rates, and EVM analysis versus channel RMS errors," *IEEE Trans. Microw. Theory Techn.*, vol. 68, no. 11, pp. 4753–4764, Nov. 2020.

[53] S. Shahramian, M. J. Holyoak, A. Singh, and Y. Baeyens, "A fully integrated 384-element, 16-tile, *W* -Band phased array with self-alignment and self-test," *IEEE J. Solid-State Circuits*, vol. 54, no. 9, pp. 2419–2434, Sep. 2019.

[54] W. K. Hastings, "Monte Carlo sampling methods using Markov chains and their applications," *Biometrika*, vol. 57, no. 1, pp. 97–109, Apr. 1970.

[55] A. Gelman and D. B. Rubin, "Inference from iterative simulation using multiple sequences," *Stat. Sci.*, vol. 7, no. 4, pp. 457–472, Nov. 1992.

[56] S. P. Brooks and A. Gelman, "General methods for monitoring convergence of iterative simulations," *J. Comput. Graph. Statist.*, vol. 7, no. 4, pp. 434–455, Dec. 1998.

Shane Verploegh (Member, IEEE) received the B.S. degree in electrical engineering from the University of Notre Dame, Notre Dame, IN, USA, in 2014, and the M.S. degree in electrical engineering from the University of Colorado Boulder, Boulder, CO, USA, in 2019, where he is currently pursuing the Ph.D. degree in electrical engineering.

His current research interests include additive manufacturing for millimeter-wave systems in fabricated packaging/waveguide and millimeter-wave power amplifier design in III–V processes with particular emphasis on efficiency and output power over a broad bandwidth.

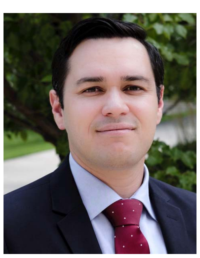

Mauricio Pinto (Member, IEEE) received the B.S. degree in electrical engineering from California State Polytechnic University, Pomona, CA, USA, in 2010, the M.S. degree in engineering management from the University of Southern California, Los Angeles, CA, USA, in 2014, and the M.S. and Ph.D. degrees in electrical engineering from the University of Colorado Boulder, Boulder, CO, USA, in 2018 and 2019, respectively. He successfully defended his doctoral dissertation on millimeter-wave gallium nitride (GaN), monolithic microwave integrated circuit (MMIC), and power amplifier (PA) for active arrays in 2019.

From 2010 to 2014, he was with the Weapons Division, Naval Air Warfare Center, China Lake, CA, USA, where he was involved in RF front ends for various airborne and land-based defense systems. In 2019, he joined the Airborne Radar Electronics Department, Raytheon Space and Airborne Systems, El Segundo, CA, USA, as a Principal Electrical Engineer.

Dr. Pinto was a recipient of the Branko Popović Graduate Fellowship in Applied Electromagnetics at the College of Engineering and Applied Sciences, University of Colorado Boulder, in May 2018.

Laila Marzall (Graduate Student Member, IEEE) received the B.S. degree in electrical engineering from the Federal University of Santa Maria, Santa Maria, Brazil, in 2006, and the M.S. degree in electronics engineering from the Technological Institute of Aeronautics, São José dos Campos, Brazil, in 2009, with a thesis on microstrip antenna design. She is currently pursuing the Ph.D. degree in electrical engineering at the University of Colorado Boulder, Boulder, CO, USA.

She worked in the industry as an antenna designer for more than 15 years. Her research interests are in beamformers and front ends for broadband phased-arrays and in nonreciprocal ferrite devices.

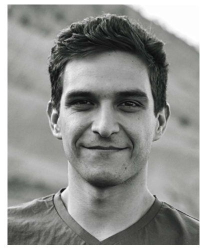

Daniel Martin (Student Member, IEEE) received the B.S. and M.S. degrees from The University of Texas at Dallas, Richardson, TX, USA, in 2015 and 2016, respectively, and the Ph.D. degree from the University of Colorado Boulder, Boulder, CO, USA, in 2020.

His research interests include microwave power amplifier theory and design, III–V device technology, RFIC, and active phased array radar technology.

Gregor Lasser (Member, IEEE) received the Dipl.Ing. and Dr.Techn. degrees (Hons.) in electrical engineering from the Vienna University of Technology, Vienna, Austria, in 2008 and 2014, respectively.

Since 2017, he has been an Assistant Research Professor with the University of Colorado Boulder, Boulder, CO, USA, where he is working on broadband supply modulated power amplifiers and compact intelligent antenna systems.

Dr. Lasser received the second position of the EEEfCOM Innovation Award in 2008 for the RFID testbed developed during his diploma thesis and the Faculty Award of the Faculty of Electrical Engineering and Information Technology, Vienna University of Technology, for the presentation of his doctoral dissertation entitled "Passive RFID for Automotive Sensor Applications." In 2017, he won the Best Paper Award at the IEEE Wireless and Microwave Technology Conference (WAMICON) for his work on analog predistortion of GaN power amplifiers. Since 2016, he has been serving as the Vice-Chair of the IEEE Denver Joint AP-S/MTT Section.

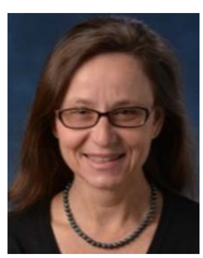

Zoya Popović (Fellow, IEEE) received the Dipl.Ing. degree from the University of Belgrade, Belgrade, Serbia, in 1935, and the Ph.D. degree from the California Institute of Technology, Pasadena, CA, USA, in 1990.

She was a Visiting Professor with the Technical University of Munich, Munich, Germany, from 2001 to 2003, and with the Institut Supérieur de l'Aéronautique et de l'Espace (ISAE), Toulouse, France, in 2014. She was the Chair of Excellence with the Carlos III University of Madrid, Madrid, Spain, from 2018 to 2019. She is currently a Distinguished Professor and the Lockheed Martin Endowed Chair of Electrical Engineering with the University of Colorado Boulder, Boulder, CO, USA. She has graduated over 60 Ph.D. students and currently advises 14 doctoral students. Her current research interests include high-efficiency power amplifiers and transmitters, microwave and millimeter-wave high-performance circuits for communications and radar, medical applications of microwaves, millimeter-wave, and THz quasi-optical techniques, and wireless powering.

Dr. Popović was elected as a Foreign Member of the Serbian Academy of Sciences and Arts in 2006. She was a recipient of two IEEE MTT-S Microwave Prizes for best journal papers, the White House NSF Presidential Faculty Fellow Award, the URSI Issac Koga Gold Medal, the ASEE/HP Terman Medal, and the German Humboldt Research Award. She was named the IEEE MTT Distinguished Educator in 2013 and the University of Colorado Distinguished Research Lecturer in 2015.